10-2024

Computational and experimental data for undoped and Er-doped lithium tantalate nanofluorescent probes

Mkhitar A. Hobosyan
The University of Texas Rio Grande Valley, mkhitar.hobosyan@utrgv.edu

Andrea Pelayo Carvajal
The University of Texas Rio Grande Valley, andrea.pelayocarvajal01@utrgv.edu

Bhupendra B. Srivastava
The University of Texas Rio Grande Valley, bhupendra.srivastava@utrgv.edu

Tamanna Zakia
The University of Texas Rio Grande Valley

Mohammed Jasim Uddin
The University of Texas Rio Grande Valley, mohammed.uddin@utrgv.edu

See next page for additional authors

Recommended Citation

Hobosyan, Mkhitar A., Andrea Pelayo Carvajal, Bhupendra B. Srivastava, Tamanna Zakia, Mohammed Jasim Uddin, Karen S. Martirosyan, Eric Rodriguez, Kofi Nketia Ackaah-Gyasi, and Nicholas Dimakis. "Computational and experimental data for undoped and Er-doped lithium tantalate nanofluorescent probes." Data in Brief 56 (2024): 110771. https://doi.org/10.1016/j.dib.2024.110771

Data in Brief 56 (2024) 110771

Contents lists available at ScienceDirect

Data in Brief

journal homepage: www.elsevier.com/locate/dib

Data Article

Computational and experimental data for undoped and Er-doped lithium tantalate nanofluorescent probes

Mkhitar A. Hobosyan[a], Andrea Pelayo Carvajal[a], Bhupendra B. Srivastava[b], Tamanna Zakia[b], Mohammed Jasim Uddin[b], Karen S. Martirosyan[a], Eric Rodriguez[c], Kofi Nketia Ackaah-Gyasi[d], Nicholas Dimakis[a,*]

[a] Department of Physics and Astronomy, UTRGV, Edinburg, TX, 78539, USA
[b] Photonics and Energy Research Laboratory-PERL, Department of Chemistry, UTRGV, Edinburg, TX, 78539, USA
[c] Department of Mechanical Engineering, University of Texas Rio Grande Valley, Edinburg, 78539, USA
[d] Department of Computer Science, University of Texas Rio Grande Valley, Edinburg, 78539, USA

ARTICLE INFO

Article history:
Received 14 April 2024
Accepted 17 July 2024
Available online 26 July 2024

Dataset link: LiTaO3-Er computational and experimental data (Original data)

Keywords:
$LiTaO_3$
Er^{+3} doping
DFT
XRD
SEM
Differential scanning calorimetry
XANES
XES

ABSTRACT

The density functional theory (DFT) and experimental data presented in this paper refer to the research article "Computational and experimental study on undoped and Er-doped lithium tantalate nano fluorescent probes". The DFT data contain electronic and optical properties for both $LiTaO_3$ and $LiTaO_3$:Er^{+3}, with Er^{+3} occupying either Li or Ta sites at 4.167 mol. %. All these properties were calculated at the generalized gradient approximation (GGA) limit. Additionally, electronic information was calculated using the hybrid functional by Heyd, Scuseria, and Ernzerho (HSE06), which accurately predicts the location in energy for all Er-4f orbitals. We also include simulated X-ray near edge (XANES) and emission spectra (XES) for the host and the doped configurations using the FEFF10 code, which provide information similar to the DFT calculated optical properties. Experimentally, we synthesized $LiTaO_3$:Er^{+3}nanoparticles, and validated them through X-ray diffraction and Scanning Electron Microscopy. We used differential scanning calorimetry and thermogravimetric analysis to confirm increases in the activation energy

* Corresponding author.
E-mail address: Nicholas.dimakis@utrgv.edu (N. Dimakis).

https://doi.org/10.1016/j.dib.2024.110771

and the lowering of the reaction temperature due to Er^{+3} doping. We collected photoluminescence data, which confirms strong f–f emission in the visible and near-infrared regions and correlates well with the HSE06 electronic information.

Specifications Table

Subject	*Physics, Chemistry*
Specific subject area	*Computational Chemistry, Materials Science*
Data format	*Raw, Analyzed*
Type of data	*Table, Figure*
Data collection	*The Vienna Ab Initio Simulation Package (VASP) was used for all density functional theory (DFT) calculations, whereas the FEFF10 code was used to produce simulated X-ray near edge (XANES) and emission spectra (XES). Experimentally, samples were analysed using X-ray diffraction (XRD), scanning electron microscopy (SEM), differential scanning calorimetry (DSC), and thermogravimetric and photoluminescence (PL) analysis. The experimental XRD files with "raw", "xy" and "xye" extensions can be read by Bruker's DIFFRAC.EVA program and with Match!.*
Data source location	*Texas Advanced Computing Center, Austin, TX 78758 and University of Texas Rio Grande Valley, Edinburg, TX 78539 and Brownsville, TX 78520*
Data accessibility	Repository name: Mendeley Data Data identification number: 10.17632/f4h6bsbbzz.2 Direct URL to data: https://data.mendeley.com/datasets/f4h6bsbbzz/2
Related research article	M.A. Hobosyan, A.P. Carvajal, B.B. Srivastava, T. Zakia, M.J. Uddin, K.S. Martirosyan, E. Rodriguez, K.N. Ackaah-Gyasi, N. Dimakis, Computational and experimental study on undoped and Er-doped lithium tantalate nanofluorescent probes, Materials Today Communications, 36 (2023) 106503 [1]. https://doi.org/10.1016/j.mtcomm.2023.106503.

1. Value of the Data

- The computational data reported are important for understanding how Er^{+3} doping in the $LiTaO_3$ (LT:Er^{+3}) at the Li and Ta locations affects the electronic and optical properties of the host ($LiTaO_3$;LT). Moreover, these data are useful to material scientists for exploring lanthanide doping on LT and other hosts.
- The simulated X-ray absorption near edge structure (XANES) and the X-ray emission spectra (XES) provide similar information as the imaginary part of the dielectric function from density functional theory calculations (DFT). When paired with densities-of-states (DOS) spectra, they provide information on the electron transition assignments for transitions between energy regions above and below the Fermi energy.
- Our experimental X-ray diffraction (XRD), scanning electron microscopy (SEM), and differential scanning calorimetry (DSC), coupled with thermogravimetric analysis (TGA) data can be used by material scientists who are developing LT nanoparticles with and without doping. The XRD for various doping concentrations provides an insight on the doping limits and its effect on LT. The SEM provides morphology information from LT:Er^{+3} nanoparticles and the DSC/TGA provides information on the reaction characteristics.
- Our approach for combining the electronic structure produced using the HSE06 functional with information from the photoluminescence spectra can serve as a reference for exploring lanthanide f−f transitions.

2. Background

Lithium tantalate ($LiTaO_3$; LT) is a nonlinear optical crystalline material that has high mechanical and chemical stability. It is widely explored for its photoelectric, piezoelectric, and ferroelectric properties. New optoelectronic properties can be achieved by doping LT with rare-earth ions. Specifically, doping LT with erbium ions (Er^{+3}) can result in strong emission in both visible and near infrared regions. This emission depends on the doping concentration. The fabrication of nanosized LT remains challenging because most methods require higher annealing temperatures with prolonged sintering time. Incorporation of Er^{+3} in the host and reduction of sintering temperature can result in nano-sized particles. An important step in receiving nano-sized particles is the transformation of initial reagents in nanoscale size domain, which can be achieved by wet chemical methods. The utilization of nanosized reagents allows lower synthesis temperatures and shorter processing times, which ultimately results in particles that are not agglomerated into larger particles.

Computational methods used verify the presence of Er-4f bands within the LT bandgap for the doped $LiTaO_3$:Er^{+3} (LT:Er^{+3}) configurations. The imaginary part of the dielectric function shows peaks in the energy region of the bandgap, which is indicative of the presence of the f–f transitions and is absent in the host spectra. An accurate estimation of the location in energy of the Er-4f bands is by using the hybrid functional HSE06. In this case, the HSE06 calculated densities-of-states (DOS) spectra are correlated with the peaks from the LT:Er^{+3} photoluminescence spectra, thus identifying the f–f transitions. The computational calculations require that Er^{+3} atoms treat the 4f states as valance states. Here, we also calculate the XANES and XES spectra, independently from DFT, which provide information on electron transitions in a similar fashion as the imaginary part of the dielectric function.

3. Data Description

The dataset in this article describes the computational and experimental data used for calculating and measuring properties, respectively, for LT and it's Er^{+3} doped counterparts LT:Er^{+3}. We consider two LT:Er^{+3} doped configurations here, both at 4.167 mol. %: The case that Er^{+3} substitutes Li (Er → Li) and the case that it substitutes Ta (Er → Ta). Fig. 1 shows the crystal side view of the optimized LT:Er^{+3} supercells used for FEFF and DFT calculations. Moreover, it also

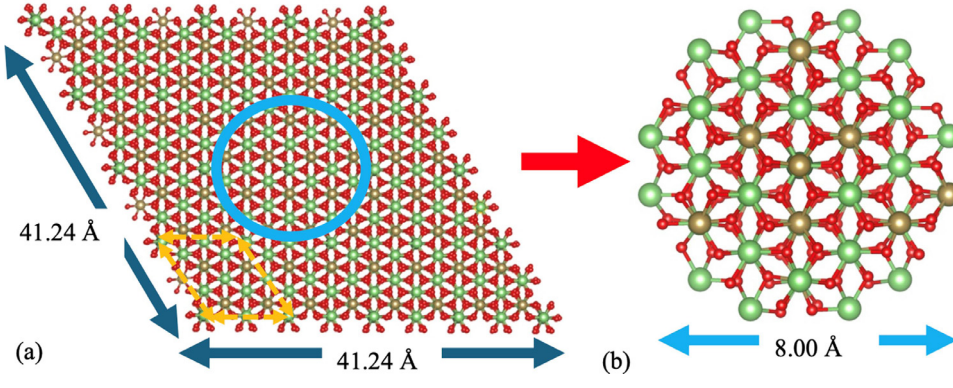

Fig. 1. (a) The top view of the $LiTaO_3$:Er^{+3} (LT:Er^{+3}) optimized 8×8×2 supercell with Er^{+3} occupying the Li site at 4.167 mol%, which is used as a starting point for FEFF10 calculations. Only atoms within the blue circle contribute to XANES and XES. The yellow arrows show the 2×2×1 supercell used for DFT calculations. (b) The final cluster around the absorbing Er^{+3} atom used for XANES and XES. Atoms are colored as follows: Li, green; Ta, brown; O, red. The Er^{+3} atoms are hidden behind the Ta and Li atoms.

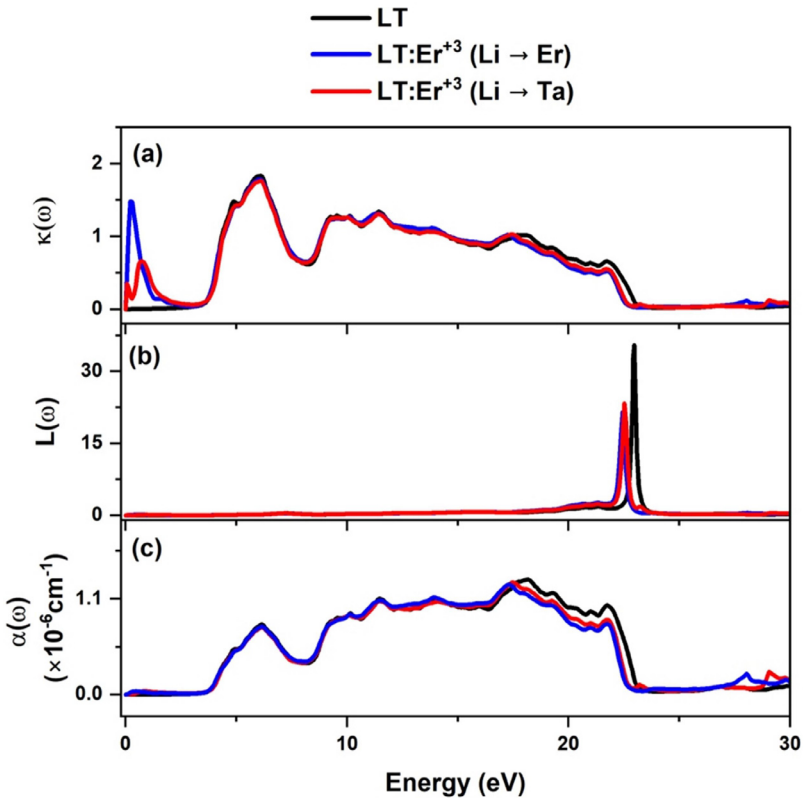

Fig. 2. a) The extinction coefficient $k(\omega)$ for LT and its Er^{+3}-doped counterparts for Er^{+3} substituting Li (Er → Li) and Ta (Er → Ta) at 4.167 mol. %, b) the loss function $L(\omega)$, and c) the absorption coefficient $\alpha(\omega)$.

shows the final cluster around the absorbing Er^{+3} atom used for XANES and XES calculations. Fig. 2 shows the extinction coefficient $k(\omega)$, the loss function $L(\omega)$, and the absorption coefficient $\alpha(\omega)$ for LT and LT:Er^{+3}, at the generalized gradient approximation (GGA) limit. Figs. 3 and 4 show the XANES and XES spectra, respectively, for the LT at the Ta L_{II}- and L_{III}-edges and for the LT:Er^{+3} at the Er M_5-edge together with the projected DOS (PDOS) per atomic orbitals. For XES, the $L_{\beta 1}$ and M_{α} lines are shown for the LT and LT:Er^{+3}, respectively. For LT:Er^{+3}, the Fermi energies are shifted to be at the middle of the Er-f band. Fig. 5 shows the XRD and SEM images exhibiting the morphology of the commercial Ta_2O_5, as well as the transformed one using the chemical treatment described in the experimental methods. The commercial powder shows strong peaks at $2\theta = 22.9^{\circ}$, 28.43°, 28.95°, 36.8°, 37.2°, 46.7°, 49.7°, 55.6°. The chemically transformed nanosized Ta_2O_5, does not show sharp peaks at any angle and has “hump” at around $2\theta = 29^{\circ}$.

Table 1 shows the bandgaps for LT and its LT:Er^{+3} doped counterparts for Er^{+3} substituting Li (Er → Li) and Ta (Er → Ta) at 4.167 mol. % for the PBE (GGA) and hybrid HSE06 functional, as well as the Er-4f locations in energy relative to the Fermi energy (E_{Fermi}) for the two LT:Er^{+3} configurations. The LT conduction band bottoms and valence band tops are also shown. Table 2 displays the DFTcalculated peak locations in energy and values for the dielectric function $\varepsilon(\omega)$, loss function $L(\omega)$, extinction coefficient $k(\omega)$, refractive index $n(\omega)$, reflectivity $R(\omega)$, absorption coefficient $\alpha(\omega)$, as well as their static values for LT and the two LT:Er^{+3} configurations. Table 3 confirms the Er-4f locations in energy relative to the Fermi energy for the LT:Er^{+3} doped configurations per magnetic quantum number, as calculated by the HSE06 functional. This in-

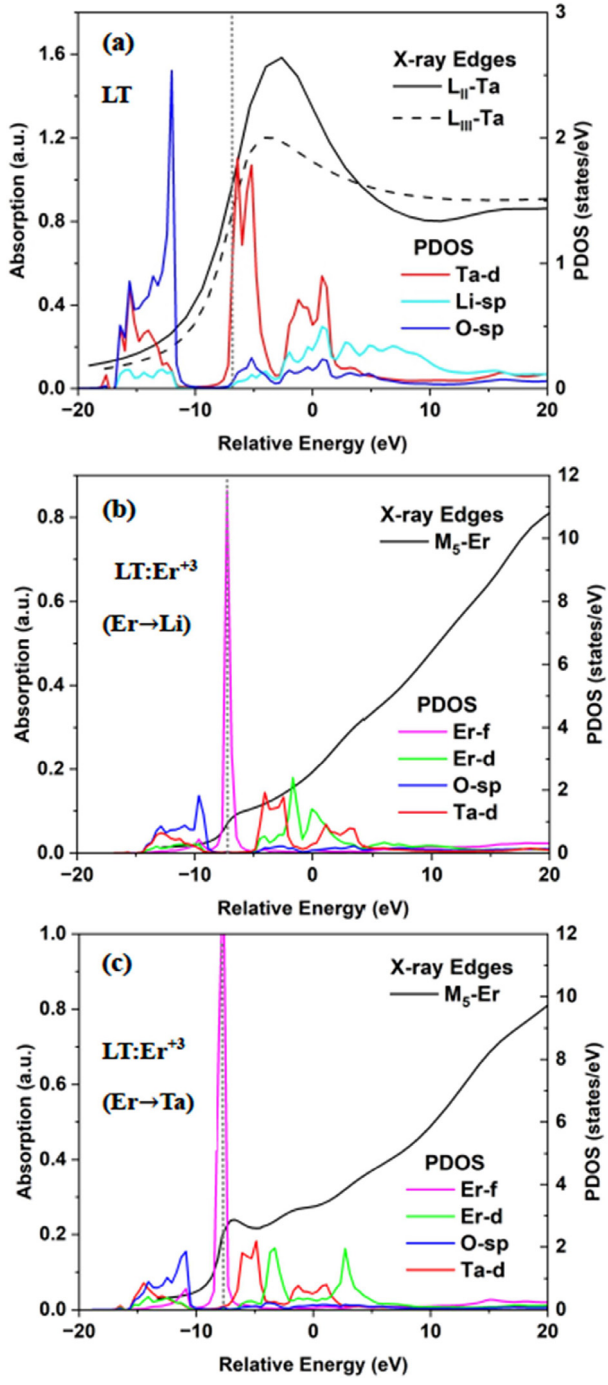

Fig. 3. The FEFF10 calculated XANES spectra for (a) the LT at the Ta L_{II}-and L_{III}-edges showing the normalized absorption (left y-axis) with respect to the energy relative to the ionization energy and projected DOS (PDOS) per Ta and O orbitals (right y-axis), (b) and (c) the LT:Er^{+3} at the Er M_5-edge also showing the PDOS for Er-f and -d orbitals. The vertical dashed line is the Fermi energy.

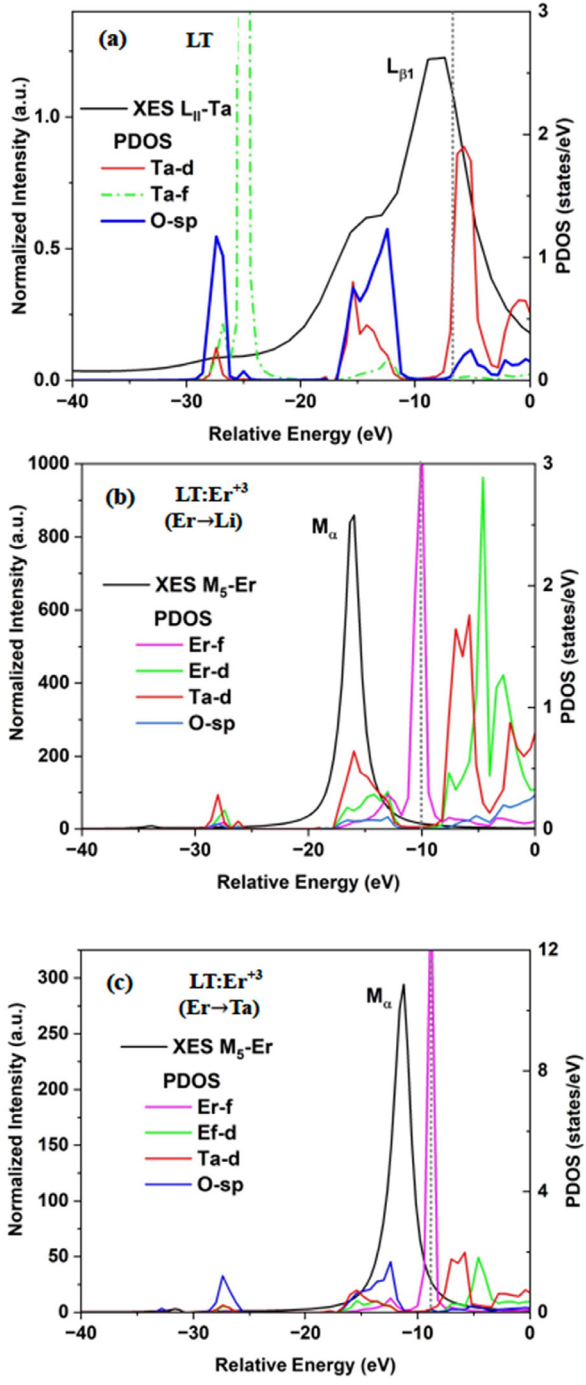

Fig. 4. The FEFF10 calculated XES spectra for (a) the LT at the Ta L_{II}-edge ($L_{\beta1}$ line) showing the normalized intensity (left y-axis) with respect to the energy relative to the ionization energy and projected DOS (PDOS) per Ta and O orbitals (right y-axis), (b) and (c) the LT:Er^{+3} at the Er^{+3} M_5-edge with the PDOS for Er-f and -d orbitals. The vertical dashed line is the Fermi energy.

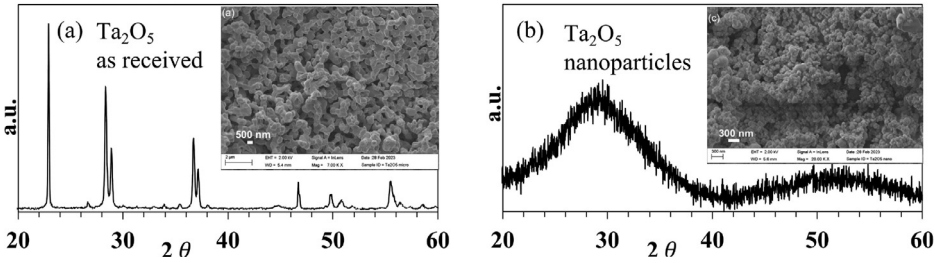

Fig. 5. XRD with corresponding SEM inset for (a) commercial Ta_2O_5 and (b) modified Ta_2O_5 nano-meter size particles.

Table 1
Electronic Bandgaps and host conduction band bottom (CBB; parenthesis) and valence band top (VBT; square brackets) for LT and its Er^{+3}-doped counterparts for Er^{+3} substituting Li (Er → Li) and Ta (Er → Ta) at 4.167 mol. % for the PBE and HSE06 functionals and the Er-4f locations in energy relative to the Fermi energy (E_{Fermi}) for the doped configurations.

Configuration	Bandgaps (eV)		$E_{Er\text{-}4f}$-E_{Fermi} (eV)	
	(CBB) [VBT]			
	PBE	HSE06	PBE	HSE06
LT	3.70 (3.65) [-0.05]	5.11 (5.07) [-0.05]		
LT:Er^{+3} (Er → Li)	3.42 (0.08) [-3.59]	0.76[1], 3.04[2] (-0.02) [-4.98]	-0.16, -0.02, 0.14	-1.87, -1.36, -0.97, -0.76, 3.93
LT:Er^{+3} (Er → Ta)	3.05 (3.09) [-0.63]	1.79[1], 3.05[2] (4.93) [0.01]	-0.50, -0.20, 0.04	-4.37, -2.94, -2.65, 1.81

[1] Close to the Fermi energy and [2] away.

Table 2
The maximum values for both the real and the imaginary parts of the dielectric function ($\varepsilon_R(\omega)_{max}$ and $\varepsilon_I(\omega)_{max}$), the loss function $L(\omega)_{max}$, the extinction coefficient $k(\omega)_{max}$, the refractive index $n(\omega)_{max}$, the reflectivity $R(\omega)_{max}$, the absorption coefficient $\alpha(\omega)_{max}$, and their static values for LT and its Er^{+3}-doped counterparts for Er^{+3} substituting Li (Er → Li) and Ta (Er → Ta) at 4.167 mol. %. Values in parenthesis refer to the locations in energy for the property maxima.

Property	Configuration		
	LT	LT (Er → Li)	LT (Er → Ta)
$\varepsilon_I(\omega)_{max}$	8.29; 8.02;4.65;3.63	7.67; 7.80;4.41;3.57	7.67; 7.57;4.53;3.47
(ω) (eV)	(4.80; 5.44;9.11;11.22)	(4.86; 5.46;9.05;11.07)	(4.86; 5.46;9.18;11.23)
$\varepsilon_R(\omega)_{max}$	10.86;3.45; 0.70	9.97;3.19;0.60	8.22; 10.14;3.21; 0.61
(ω) (eV)	(4.11;8.71; 10.73)	(4.03;8.65; 10.66)	(0.46; 4.18; 8.69; 10.73)
$\varepsilon_R(0)$	5.15	18.44	10.13
$L(\omega)_{max}$	35.10	21.48	23.06
(ω) (eV)	(22.97)	(22.44)	(22.51)
$\boldsymbol{\alpha}$ $(\omega)_{max}$ (x10^{-6}cm^{-1})	0.82; 1.12; 1.32; 1.04	0.79; 1.13; 1.26;0.88	0.77; 1.07; 1.28; 0.83
(ω) (eV)	6.16; 11.46; 18.08; 21.77	6.15; 13.93; 17.29;21.74	6.15; 11.50; 17.51; 21.76
$k(\omega)_{max}$	1.83; 1.34; 1.03; 0.66	1.78; 1.32; 1.03; 0.53	1.75; 1.32; 1.04; 0.56
(ω) (eV)	6.12; 11.45; 17.93; 21.73	6.04; 11.38; 17.28; 21.71	6.12; 11.42; 17.44; 21.72
$n(\omega)_{max}$	3.36; 2.06; 1.46; 0.92	3.22; 2.00; 1.43;0.82	3.24; 2.00; 1.41; 0.87
(ω) (eV)	4.16; 8.80; 10.82;16.79	4.09;8.77; 10.78; 16.67	4.22; 8.78; 10.82; 16.76
$n(0)$	2.25	4.31	3.04
$R(\omega)_{max}$ (%)	36.33; 27.61; 36.58; 77.19	34.89;27.03; 37.52; 64.21	34.66; 26.60; 36.90; 67.91
(ω) (eV)	6.18; 11.58; 19.52; 22.64	6.18; 11.60; 19.65; 22.21	6.19; 11.57; 19.58; 22.27
$R(0)$	14.27	39.67	26.27

Table 3
The Er-4f locations in energy relative to the Fermi energy (E_{Fermi}) for the doped configurations per magnetic quantum number m_l as calculated by the HSE06 functional through densities of states.

Configuration	$E_{Er\text{-}4f}$-E_{Fermi} (eV)			
	$4f_{z^3}$ ($m_l = 0$)	$4f_{xz^2} + 4f_{yz^2}$ ($m_l = \pm 1$)	$4f_{xyz} + 4f_{zx^2}$ ($m_l = \pm 2$)	$4f_{y^3x^2} + 4f_{x^3}$ ($m_l = \pm 3$)
LT:Er^{+3} (Er → Li)	-1.84	-1.91, -1.38, 3.92, 4.05	-1.91, -1.38, 3.92, 4.05	-0.98, -0.78
LT:Er^{+3} (Er → Ta)	-4.32	-4.38, 1.78	-4.38, 1.78	-2.92, -2.68

Table 4
Fluorescence spectra peak locations assignments in the visible region and the near IR per Er^{+3} f–f transition assignment for LT:Er^{+3} under 0.5, 3, and 10 mol. % of Er_2O_3.

Er_2O_3 mol. % concentration	Fluorescence spectra peak locations per Er^{+3} f–f transition assignment (nm)			
	$^2H_{11/2} \rightarrow {}^4I_{15/2}$	$^4S_{3/2} \rightarrow {}^4I_{15/2}$	$^4F_{9/2} \rightarrow {}^4I_{15/2}$	$^4I_{13/2} \rightarrow {}^4I_{15/2}$
0.5	527[1]	548[1]	654, 668[1]	1483, 1514, 1527[1], 1541, 1562, 1578
3	524[1], 529, 534	548[1], 557	656, 661, 671[1]	1483, 1514, 1527[1], 1541, 1562, 1578
10	Not observed	Not observed	654, 672[1]	1528[1]

[1] most prominent peak.

Table 5
XRD peak intensities and 2θ locations for experimental and DFT-calculated LT:Er^{+3}.

Experimental								Computational	
LT		(0.5% Er)		(3% Er)		(10% Er)		(Er → Li)	
2θ (°)	Intensity	2θ (°)	Intensity	2θ (°)	Intensity	2θ (°)	Intensity	2θ (°)	Intensity
23.791	100.00	23.731	100.00	23.893	100.00	23.772	100.00	23.67	100.00
32.866	37.219	32.826	35.270	33.008	33.672	32.866	36.849	32.64	33.637
34.811	26.581	34.77	24.571	34.973	22.432	34.811	23.315	34.77	22.402
39.247	5.901	39.226	4.941	39.368	4.748	39.267	5.305	38.87	3.408
40.158	4.721	40.138	3.593	40.259	4.016	40.178	4.001	40.00	1.937
42.649	13.264	42.528	12.206	42.67	10.772	42.528	11.915	42.50	10.74
48.645	14.109	48.564	12.325	48.726	10.928	48.584	12.418	48.43	9.78
53.466	16.911	53.385	15.614	53.547	13.558	53.466	15.113	53.13	13.343
56.079	10.657	56.099	9.736	56.221	8.406	56.14	10.166	56.03	8.287
57.375	6.289	57.274	5.324	57.456	4.732	57.375	6.237	56.85	3.890

Table 6
Thermogravimetric analysis for peak temperature, weight loss and energy release/absorption at various temperature ranges for Ta_2O_5-LiOH and Ta_2O_5-LiOH-3mol% Er_2O_3 formulations.

Thermogravimetric analysis				
Range (°C)	Sample	Peak (°C)	Energy release (J/g)	Weight loss (%)
0-400.0	Ta_2O_5-LiOH	-	-	9.7
	Ta_2O_5-LiOH - 3 mol% Er_2O_3	-	-	6.9
400.0-700.0	Ta_2O_5-LiOH	618.7	132.5	1.24
	Ta_2O_5-LiOH - 3 mol% Er_2O_3	585.3	121.9	0.46
700.0-1100.0	Ta_2O_5-LiOH	888	2974	-
	Ta_2O_5-LiOH - 3 mol% Er_2O_3	893	2879	-

formation has been extracted from the DFT-calculated DOS spectrum. Table 4 shows the fluorescence spectra peak locations assignments in the visible region and the near IR per Er^{+3} f–f transition assignment for LT:Er^{+3} at 0.5, 3, and 10 mol. % of Er_2O_3. Table 4 information was obtained using photoluminescence spectra. Table 5 shows the XRD peaks and their locations for our experimental and simulated data for LT:Er^{+3}. The small changes in the peak locations show that doping minimally affects the lattice parameters and atomic positions. Table 6

shows the thermogravimetric analysis (TGA) for LT and LT:Er^{+3} at 3 mol. % of Er_2O_3. The initial weight loss from both samples, within the ranges of 0-400°C, is due to the evaporation of remnant solvents and water from the transformed Ta_2O_5. In 400-700°C, both samples exhibit an exothermic reaction and a minor weight loss, which indicates that the reaction is not completed. Lastly, for temperature ranges 700-1100°C an exothermic effect is detected with no weight loss, which is indicative of crystallization. The TGA analysis shows the similar nature of both samples.

The submitted data are grouped in two directories, one for the experimental data and the one for the computational data. The experimental data directory contains four subdirectories, with data from photoluminescence, XRD, SEM, and TGA experiments and a word document, which provides a short description for the files per subdirectory. The SEM and TGA only contain image files in TIF format. The computational data directory contains three subdirectories, one for the host LT and two for the LT:Er^{+3} doped configurations. Each of these contain six subdirectories, two for bands structure and DOS calculations (one for GGA and another for HSE06), one for optical properties, one for the Bader-type charges, one for XANES, and one for XES. The subdirectories, which relate to DFT calculations, contain VASP input and output files from these calculations (raw data), whereas the XANES and XES contain all FEFF10 input and output files. The folders that contain band structure raw data also contain processed files. The optical properties subdirectory for the LT also contains the processed optical properties file for the LT and LT:Er^{+3}.

4. Experimental Design, Materials and Methods

Supercell modelling for DFT calculations. The DFT-optimized $2 \times 2 \times 1$ supercell for LT:Er^{+3} with Er^{+3} substituting Li (Er → Li) at 4.167 mol. % is shown in Fig. 1a (yellow arrows) This supercell has 1 Er, 23 Li, 24 Ta and 72 O atoms (120 atoms in total) and is in a triclinic form (space group *R3c*). Fig. 1b shows that each Li and Ta atom are coordinated with six oxygens in an octahedral configuration, whereas the same applies for the Er-O coordination geometries.

DFT code and parameters. The code Vienna *Ab initio* Simulation Package (VASP version 6) [2-5] was used for the DFT calculations of the electronic structure, optimal geometries, and optical properties for the LT and its Er^{+3}-doped counterparts. The projector augmented-wave (PAW) pseudopotentials were used for Li, Ta, O, and Er. The effective valences of the Li, Ta, O, and Er are $2s^1$, $5d^46s^1$, $2s^22p^4$, $4f^{11}5s^26s^25p^65d^1$. The DFT Kohn–Sham equations are solved using GGA under the Perdew–Burke–Ernzerhof (PBE) functional [6]. We used the hybrid functional HSE06 by Heyd, Scuseria, and Ernzerho (HSE06) for electronic information calculations due to its improved bandgaps [7-11]. Long-range (i.e., van der Waals) interactions were included in our calculations through the D3 semiempirical correction by Grimme [12]. The kinetic energy cut-off value for all calculations is 600 eV, which larger than the VASP recommended value of 520 eV for this work. The recommended value is calculated as 1.3 times the larger energy cut-off value from the elements used in this work, which is O with $E_{cutoff} = 400\ eV$. The energy and the geometry optimization convergence criteria were set at 10^{-9} eV and 10^{-4} eV/Å per atom, respectively. The Brillouin-zone (BZ) was sampled using the Γ-centred 6×6×6 Brillouin zone (BZ) grid.

The Bader Charge Analysis code by Henkelman and co-workers [13-16] was used to calculate Bader-type ion charges. This code partitions the charge density grid into Bader-type volumes and scales linearly with the number of grid points. Thus, it can be used by large supercells.

The frequency-dependent dielectric function is written as:

$$\varepsilon(\omega) = \varepsilon_R(\omega) + i\varepsilon_I(\omega) \tag{1}$$

where $\varepsilon_R(\omega)$ and $\varepsilon_I(\omega)$ are its real and imaginary parts, respectively, and ω is the photon energy. The refractive index $n(\omega)$, the extinction coefficient $k(\omega)$, the reflectivity $R(\omega)$, and the

energy-loss function $L(\omega)$, are given in terms of $\varepsilon_R(\omega)$, $\varepsilon_I(\omega)$, $n(\omega)$, and $k(\omega)$ as follows:

$$n(\omega) = \left(\frac{[\varepsilon_R(\omega)^2 + \varepsilon_1(\omega)^2]^{\frac{1}{2}} + \varepsilon_R(\omega)}{2} \right)^{\frac{1}{2}}, \tag{2}$$

$$k(\omega) = \left(\frac{[\varepsilon_R(\omega)^2 + \varepsilon_1(\omega)^2]^{\frac{1}{2}} - \varepsilon_R(\omega)}{2} \right)^{\frac{1}{2}}, \tag{3}$$

$$R(\omega) = \frac{(n(\omega) - 1)^2 + k(\omega)^2}{(n(\omega) + 1)^2 + k(\omega)^2}. \tag{4}$$

$$L(\omega) = \frac{\varepsilon_1(\omega)}{\varepsilon_R(\omega)^2 + \varepsilon_1(\omega)^2}. \tag{5}$$

The VASP calculated optical properties require several conduction bands in the calculations. Here, the ground state calculations for the doped configurations used 359 bands, whereas 640 bands were employed for the corresponding optical properties calculations. The independent particle approximation (IPA) [17] was used here under the exact diagonalization algorithm. The reported optical properties are averaged over the corresponding components parallel to x, y, and z axis.

XANES and XES calculations. XANES and XES spectra were obtained using the FEFF10 code, which employs real space Green functions. For both cases, the atomic potentials and the Fermi energies were calculated self-consistently. Full multiple scattering is included in the calculations. The exchange interaction was obtained using the Hedin-Lundqvist pseudopotentials. The absorbing atom core-hole was treated at the random phase approximation (RPA) level. FEFF10 calculates atomic charges and DOS (total and projected per atom and orbital), in a similar fashion as DFT.

Synthesis of LT doped with various molar concentrations of Er^{+3}. Lithium tantalate nanoparticles containing various molar concentrations of Er^{+3} were synthesized using wet chemical synthesis method. In this case, tantalum oxide was first transformed to nm domain by dissolving 0.28 g of Ta_2O_5 in 5 ml of 48% HF in a water heat bath at 75 °C for 8 hr, then neutralizing it with ammonium hydroxide 30% solution, washing with deionized water, and centrifuging 3 times, followed by drying in an oven at 100 °C for 12 hours. The as-prepared Ta_2O_5 was mixed with stoichiometric amount of LiOH and 0.5–10 mol. % of Er_2O_3 in acetone with zirconia balls using the High Energy Ball Mill (HSF-3, MTI Co) machine for 5 minutes. The homogenized mixture was air dried, placed in the oven (GSL-1100X, MTI), which was programmed to reach 650 °C in 50 minutes and was kept at 650 °C for 4 hours, yielding the desired product with corresponding erbium doping concentrations.

XRD, SEM, and DSC/TGA analysis of reagents and reaction products. The initial mixture was analysed using differential scanning calorimetry and thermogravimetric analysis method (DSC/TGA, Q-600, TA Instruments). In this method, a small amount (10-15 mg) of initial powder mixture containing as-prepared Ta_2O_5, LiOH and 0.5–10 mol. % of Er_2O_3 was heated at 20°C/min heating rate until temperature reached 1100 °C. During heating, the weight and heat flow were continually measured with high precision (0.1 microgram sensitivity for weight and 0.001°C for temperature sensitivity). The exotherm and endotherm effects were measured by integrating the DTA heat flow curve for the corresponding temperature region. The activation energy of the samples was calculated using the peak temperature values taken from the heat flow curve, for heating rates between 15–30°C/min, using the isoconversional method suggested by Starink [18,19].

The activation energy was determined according to the following equation:

$$ln\left\{ \frac{T^{1.8}}{\beta} \right\} = \left(1.007 - 1.2 \times 10^{-5} E_a\right) \frac{E_a}{RT} + const \tag{6}$$

where E_a is the apparent activation energy (in kJ/mol), β is the heating rate used in thermal analysis (in K/min), T is the peak temperature of the exothermic curve (in K), and R is the universal gas constant. The E_a is estimated from the slope of $ln(T^{1.8}/\beta)$ vs. $1/T$. We estimated the activation energy in the Ta_2O_5-LiOH to be 138 kJ/mol, while the activation energy for the Ta_2O_5-LiOH-3 mol. % Er_2O_3 system was 263 kJ/mol.

The XRD analysis of samples was carried out in Bruker D-2 Phaser with Cu K_α anode, in the 2θ range of 20–80°. The XRD scans were taken with θ precision of 0.02° and the sample was rotated with 15 rpm to statistically increase the number of particles contributing to the XRD signal intensity. The morphology of the particles was examined using SEM (JEOL, JSM-7100F).

Limitations

The optical properties calculations use IPA due to RAM limitations. RPA would increase the accuracy of the optical properties, but it would require more than 20 TBytes of RAM under the current VASP parameters.

The XRD experimental measurements have limitations in detecting less than 1 wt. % impurities, depending on the nature and crystallinity of the specific impurity. SEM analysis have limitations on magnification, which depends on the particle size and charging of the particles, as well as vibrations at high magnifications. DSC/TGA analysis is limited to temperature range between room temperature to 1450 °C, which limits material examination above this temperature.

Ethics Statement

The authors have read and follow the ethical requirements for publication in Data in Brief and confirming that the current work does not involve human subjects, animal experiments, or any data collected from social media platforms.

Credit Author Statement

Mkhitar A. Hobosyan: Conceptualization, Methodology, Data curation, Supervision, Validation, Resources, Writing, reviewing, and editing; **Andrea Pelayo Carvajal:** Data curation, Validation, Resources; **Bhupendra Srivastava**: Data curation, Validation, Resources; **Tamanna Zakia:** Data curation, Validation, Resources; **Mohammed Jassim Uddin**: Data curation, Validation, Resources; **Karen S. Martirosyan**: Data curation, Validation, Resources; **Eric Rodriguez**: Data curation, Validation, Resources; **Kofi Nketia Ackaah-Gyasi**: Data curation, Validation, Resources **Nicholas Dimakis**: Conceptualization, Methodology, Calculations, Supervision, Validation, Resources, Writing, reviewing, and editing.

Data Availability

LiTaO3-Er computational and experimental data (Original data) (Mendeley Data).

Acknowledgements

The author(s) would like to acknowledge funding provided by the National Science Foundation CREST Center for Multidisciplinary Research Excellence in Cyber-Physical Infrastructure Systems (NSF Award No. 2112650). The opinions expressed in this paper (or thesis or report or dissertation) are solely those of the author(s), and do not necessarily represent those of the NSF.

The authors also acknowledge the Texas Advanced Computing Center (TACC) at The University of Texas at Austin for providing HPC resources that have contributed to the research results reported within this paper. URL: http://www.tacc.utexas.edu.

Declaration of Competing Interest

The authors declare that they have no known competing financial interests or personal relationships that could have appeared to influence the work reported in this paper.

References

[1] M.A. Hobosyan, A.P. Carvajal, B.B. Srivastava, T. Zakia, M.J. Uddin, K.S. Martirosyan, E. Rodriguez, K.N. Ackaah-Gyasi, N. Dimakis, Computational and experimental study on undoped and Er-doped lithium tantalate nanofluorescent probes, Mater. Today Commun. 36 (2023) 106503.
[2] G. Kresse, J. Hafner, Ab initio molecular dynamics for liquid metals, Phys. Rev. B 47 (1993) 558(R)-561(R).
[3] G. Kresse, J. Hafner, Ab initio molecular-dynamics simulation of the liquid-metal–amorphous-semiconductor transition in germanium, Phys. Rev. B 49 (1994) 14251–14269.
[4] G. Kresse, J. Furthmüller, Efficiency of ab-initio total energy calculations for metals and semiconductors using a plane-wave basis set, Comput. Mater. Sci. 6 (1996) 15–50.
[5] G. Kresse, J. Furthmüller, Efficient iterative schemes for ab initio total-energy calculations using a plane-wave basis set, Phys. Rev. B 54 (1996) 11169–11186.
[6] J.P. Perdew, K. Burke, M. Ernzerhof, Generalized gradient approximation made simple, Phys. Rev. Lett. 77 (1996) 3865.
[7] A.V. Krukau, O.A. Vydrov, A.F. Izmaylov, G.E. Scuseria, Influence of the exchange screening parameter on the performance of screened hybrid functionals, J. Chem. Phys. 125 (2006) 224106-224105.
[8] W. Kohn, L.J. Sham, Self-consistent equations including exchange and correlation effects, Phys. Rev. 140 (1965) A1133.
[9] A.J. Garza, G.E. Scuseria, Predicting band gaps with hybrid density functionals, J. Phys. Chem. Lett. 7 (2016) 4165–4170.
[10] P. Hohenberg, W. Kohn, Inhomogeneous electron gas, Phys. Rev. 136 (1964) B864.
[11] J. Heyd, G.E. Scuseria, M. Ernzerhof, Hybrid functionals based on a screened Coulomb potential, J. Chem. Phys. 118 (2003) 8207–8215.
[12] S. Grimme, J. Antony, S. Ehrlich, H. Krieg, A consistent and accurate ab initio parametrization of density functional dispersion correction (DFT-D) for the 94 elements H-Pu, J. Chem. Phys. 132 (2010) 154104–154119.
[13] W. Tang, E. Sanville, G. Henkelman, A grid-based Bader analysis algorithm without lattice bias, J. Phys. Condens. Matter 21 (2009) 084204.
[14] E. Sanville, S.D. Kenny, R. Smith, G. Henkelman, Improved grid-based algorithm for Bader charge allocation, J. Comput. Chem. 28 (2007) 899–908.
[15] G. Henkelman, A. Arnaldsson, H. Jónsson, A fast and robust algorithm for Bader decomposition of charge density, Comput. Mater. Sci. 36 (2006) 354–360.
[16] M. Yu, D.R. Trinkle, Accurate and efficient algorithm for Bader charge integration, J. Chem. Phys. 134 (2011) 064111.
[17] S.L. Adler, Quantum theory of the dielectric constant in real solids, Phys. Rev. 126 (1962) 413–420.
[18] M.J. Starink, The determination of activation energy from linear heating rate experiments: a comparison of the accuracy of isoconversion methods, Thermochim. Acta 404 (2003) 163–176.
[19] M.A. Hobosyan, K.G. Kirakosyan, S.L. Kharatyan, K.S. Martirosyan, PTFE–Al_2O_3 reactive interaction at high heating rates, J. Therm. Anal. Calorim. 119 (2015) 245–251.